Self-ordered electrochemical growth on single-crystal electrode surfaces

Self-ordered electrochemical growth on single-crystal electrode surfaces

Philippe Allongue[1] and Fouad Maroun

Laboratoire de Physique de la Matière Condensée (UMR 7643 CNRS), Ecole Polytechnique,
F-91128 Palaiseau, France

E-mail: Philippe.Allongue@Polytechnique.edu

Abstract

This paper is a brief review of self-ordered electrochemical growth on single-crystal electrode surfaces on which arrays of nanostructures are created by replication of patterns made by atomic steps or surface reconstruction. Whenever possible the parallel is made between electrochemical growth and molecular beam epitaxy in ultrahigh vacuum. An atomistic view of electrodeposition is given first to help with identifying the similarities of and specific differences between the two techniques of growth. Recent examples where self-organized nanostructures are prepared on metals and silicon substrates are discussed.

(Some figures in this article are in colour only in the electronic version)

1. Introduction

While the 'top-down' approach based on continuous advances in lithography is almost reaching its ultimate limit, future trends are giving a rising importance to the 'bottom-up' approach, because self-assembling processes of elementary building blocks, from atoms and small molecules to more complex entities such as biomolecules and nanoparticles, have made important progress during the past few decades [1]. Molecular self-organization on surfaces is well established and it originates from lateral interactions between the adsorbed species and minimization of the surface energy of the system by increasing local packing. In crystal growth the atoms self-assemble into extremely well defined lattices due to short range forces, but the nucleation stage is essentially a random process on a defect free substrate. Fortunately there exist on real single-crystal surfaces defect sites that are energetically more favourable for the incorporation of the foreign adatoms. Hence, the self-ordered growth of nanostructures primarily relies on our ability to create natural or artificial atomic scale templates on surfaces

---

[1] Author to whom any correspondence should be addressed.

and then find conditions for replicating them by preferential nucleation and controlled growth. Natural surface defects include step edges, atomic vacancies and dislocations.

The growth of self-ordered nanostructures was primarily developed by the ultrahigh vacuum (UHV) community after decades dedicated to surface science studies and increasing knowledge in the preparation of surfaces with ever better controlled in plane structure. We give below only a brief overview of most significant achievements and the reader should refer to other contributions in this Special Issue for more details. The clean Si(111) surface with the 7×7 reconstruction is probably the prototype of the clean surface studied in UHV. Several examples show that its large surface unit cell may be used to create regular arrays of magic clusters with Al, Ga and In [2]. Moreover, careful choice of the miscut angle and orientation of the Si(111) surface allows obtaining quasi-perfect stepped surfaces, where the 7×7 reconstruction plays a major role in the morphology, separation and height of the steps. Vicinal Si(111) surfaces were used as templates for the deposition of 1D metallic nanostructures [3], chains of nanoparticles [4] and nanowires [5]. Vicinal metal surfaces may also be used as templates. For instance Co atomic chains, with one atomic row to several atomic rows in width, were prepared on Pt(788) by precise step edge decoration [6]. A square lattice of size monodisperse Co dots was obtained on reconstructed Au(788) after careful optimization of the growth conditions [7]. The domain boundaries of the $22 \times \sqrt{3}$ surface reconstruction of *flat* Au(111) terraces build a herringbone pattern, with surface dislocations at the elbows. The resulting $63 \text{ Å} \times 150 \text{ Å}$ rectangular pattern was replicated with nanostructures for metals with a higher surface energy than gold [8–12]. In the case of unreconstructed clean metal surfaces, artificial heterogeneity patterns were generated by different methods. A first approach is creating a periodic dislocation network by depositing a foreign metal with a large lattice mismatch with respect to the substrate. A very nice example of this kind is provided by the system Ag/Pt(111) for which the deposition of two silver monolayers promotes a very regular dislocation network [13] which served as template for growing a high density array of Fe nanostructures [14]. Here the dislocation lines act as barriers against adatom diffusion, confining them within the triangular regions delimited by the dislocations. A second method uses the chemical modifications of a surface. Nitrogen adsorption on Cu(100) leads for instance to a square template which was used to grow self-organized Au nanodots since gold does not deposit on the N layer [15]. A third surface patterning method is based argon implantation followed by appropriate annealing. In the case of Ru(0001), the technique leads to a regular hexagonal pattern with heterogeneous catalytic reactivity [16]. This method could be attempted in crystal growth.

Electrodeposition is an alternative technique of crystal growth, which is widely used in industry, including microelectronics, because large and uniform deposition rates are attainable, on surfaces with complicated shapes. In the past few decades an atomistic view of electrodeposition has emerged thanks to two important breakthroughs. The first one concerns the preparation of clean *reconstructed* surfaces of noble metal single crystals at ambient by annealing in a butane or a hydrogen flame: this technique is called 'flame annealing' and it works principally with Au and Pt [17]. The second one concerns the advent of the electrochemical STM for *in situ* real time observations of surface processes with the atomic resolution at metal [18–21] and semiconductor electrodes [22]. During the past two decades numerous fundamental *in situ* STM studies have focused on the growth mechanisms of high quality ultrathin epitaxial layers on single-crystal surfaces for their specific catalytic, corrosion protection and magnetic properties.

In the present paper we focus on *self-ordered* metal electrodeposition by replication of patterns created on single-crystal electrode surfaces and attempt to discuss the similarities with and the differences from the parent technique in UHV. The prerequisite is, like for
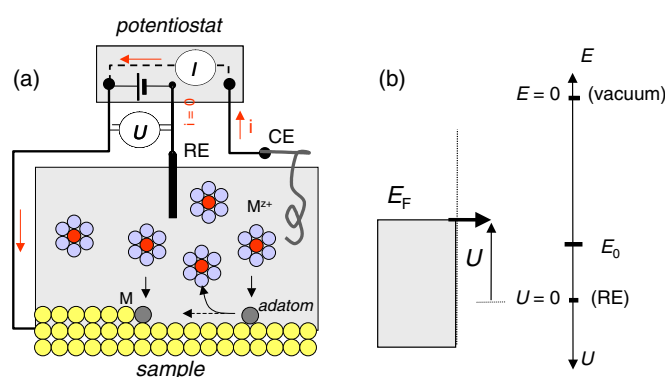
Figure 1. (a) Three-electrode experimental set-up used for electrochemical deposition. RE and CE designate the reference electrode and counter-electrode. On the molecular scale the process involves the adsorption of an adatom whose lifetime and effective diffusion length on the surface depends on the applied potential. At *low* overpotential the adatom may desorb because it is in equilibrium with the solution. At large overpotential the adatom is *irreversibly* adsorbed. (b) Simplified energy diagram of the metal–electrolyte junction explaining the polarization conditions required for metal deposition: the metal Fermi level E_F must be *above* E_0 in the energy scale or, equivalently, the applied potential U must be more negative than E_0.

UHV deposition, preparing metal or semiconductor electrode surfaces with a periodic pattern and maintaining it in the electrochemical environment prior to deposition. All successful attempts described below are closely related to a deep know-how concerning the surface preparation of substrates. We have chosen to discard from this short review cases where the self-organization is arising from deposition through a mask. One of the best known examples of this kind is the electrodeposition of nanowires [23–25] inside self-organized nm pores made in Al_2O_3 by anodization of aluminium [26, 27]. Another important example is templated electrocrystallization through self-assembled polystyrene beads [28]. Both cases demonstrate that electrodeposition is an ideal method for filling in complex cavities down to the nm scale.

The paper is organized as follows. In a first section we give a brief atomistic view of electrodeposition and discuss the main parameters controlling the nucleation and growth modes at the electrochemical interface. Self-ordered electrodeposition of metals on metal and silicon electrode surfaces is then discussed in two distinct sections. In the case of silicon a subsection addresses the question of the surface preparation.

2. A brief atomistic view of metal electrodeposition

Electrodeposition consists in reducing the ionic metal species dissolved in an electrolyte by transfer of one or several electrons from the substrate according to the total reaction $M^{Z+} + ze^- \rightarrow M$. Electrodeposition is performed with a three-electrode electrochemical cell connected to a potentiostat (figure 1(a)): the substrate potential is applied with respect to the reference electrode, a well defined redox system that defines the origin of the potential scale on the solution side. The counter-electrode, often made of an inert metal, is an auxiliary electrode closing the external electrical circuit. Details about the principle of a potentiostat can be found in textbooks [29]. In the energy diagram of figure 1(b) the correspondence between the energy scale ($E = 0$ refers to vacuum) and the potential scale ($U = 0$ is given from the redox system used as reference) can be determined experimentally. This simplified scheme readily explains that metal electrodeposition requires applying an electrode potential U more negative than the standard redox potential $E_0 = E(M^{Z+}/M)$.
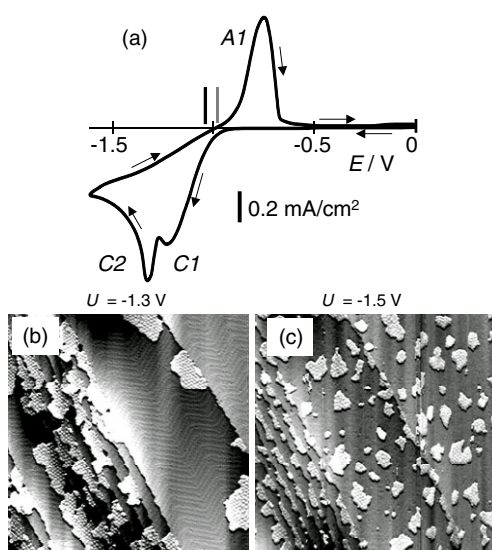
Figure 2. (a) Voltammogram of a Au(111) electrode in a CoSO$_4$ solution of pH 4 (sweep rate 50 mV s^{-1}) [31]. See the text for the assignment of the different current peaks. The black and light grey vertical bars respectively mark the positions of the standard potentials $E(Co^{2+}/Co)$ and $E(H^+/H_2)$ of the solution. ((b), (c)) *In situ* STM (150 nm $\times$ 150 nm) showing the initial stages of nucleation [30]. The images were recorded after 4 s of cobalt deposition at -1.3 V (b) and -1.5 V (c). Note the different morphologies obtained: step flow growth at the step edges in (b) and homogeneous nucleation on atomically smooth terraces in (c).

To characterize the kinetics of the electrodeposition process one records a voltammogram, i.e. the variations of the current as a function of the applied potential. An example is given in figure 2(a) for the system CoSO$_4$–Au(111): when sweeping the potential from 0 V, where no reaction occurs ($i \sim 0$), to -1.6 V the two negative peaks of current stand for two reactions: C1 originates from the reduction of the protons into molecular H$_2$ (H$^+$ + e$^-$ $\rightarrow$ $\frac{1}{2}$H$_2$; $E_0 = E(H^+/H_2) = -0.92$ V$_{MSE}$) and C2 corresponds to the reduction of Co^{2+} ions into metallic cobalt (Co^{2+} + 2e$^-$ $\rightarrow$ Co, $E_0 = E(Co^{2+}/Co) = -1.01$ V$_{MSE}$). Note that this second reaction occurs in parallel with the first one. On the positive going sweep of potential -1.6 V $\rightarrow$ 0 V, the positive peak of current A1 stands for the dissolution of the cobalt layer which was deposited (Co $\rightarrow$ Co^{2+} + 2e for $U > E(Co^{2+}/Co)$). Hence a voltammogram primarily yields information about the nature of the surface reactions. Because the electron transfer is an activated process the deposition current varies as $\sim \exp(-\alpha z \eta / kT)$ [29] for small overpotentials $\eta = E_0 - U$ (>0): α is the transfer coefficient ($0 < \alpha < 1$) and E_0 stands for the standard redox potential of the reaction considered. The deposition flux is therefore potential controlled and its exponential dependence on the overpotential offers a large dynamic of fluxes. Above a critical value of η the current becomes however essentially limited by the transport of the metallic ions from the bulk of the solution towards the electrode surface. The electrochemical transfer is said to be limited by mass transport.

This phenomenon lies at the origin of the shape of the cathodic peaks C1 and C2. Figures 2(b), (c) present two *in situ* STM images where cobalt was deposited on reconstructed Au(111) for 4s and at different potentials [30]. Likewise in UHV, the cobalt islands are all biatomic in height [10]. The difference from MBE is however manifest since the cobalt islands are nucleating at the gold step edges when the potential is close to $E(Co^{2+}/Co)$ (figure 2(b)) or

are nucleating homogeneously on the gold (111) terraces at a larger overpotential (figure 2(c)). In UHV, place exchange is systematically observed at the elbows of the reconstruction pattern (note that place exchange may be also observed in the electrochemical environment under certain conditions; see the next section). At both potentials an atomically smooth Co(0001) film is then obtained in a layer by layer fashion [31, 32] whereas a rather 3D growth of Co(0001) is promoted in UHV after the place exchange nucleation process [10]. It should be mentioned that the above 2D cobalt growth mechanism is specific to the sulfate solution and that the addition of trace amounts of other anions may considerably alter the growth modes. For instance the addition of thiocyanates (SCN^-) in the above sulfate cobalt solution promotes a 3D growth [33]. More generally, quite different nucleation and growth modes may be obtained for a given metal via an appropriate choice of the solution composition and applied potential, which makes electrodeposition a versatile deposition technique.

On the molecular scale, electrodeposition involves the adsorption of an adatom (figure 1(a)) whose lifetime on the surface critically depends on the applied potential. The rate of adsorption equals that of desorption when $U = E_0$ ($\eta = 0$) which may lead to strong surface restructuring in some cases (e.g. Cu, Ag). As soon as $\eta > 0$ (towards deposition) the adatom desorption probability decreases rapidly and the process competes with surface diffusion. In cases where the adsorption step is highly site dependent (the case of heterogeneous kinetics on the atomic scale) deposition occurs directly on the corresponding specific surface sites without any surface diffusion. This mechanism, which may be observed only at small η, is called *direct* deposition. An illustration of this mechanism is given by figure 2(b) where the deposition initiated from the step edges. The direct deposition mechanism has no equivalent in MBE growth. Increasing η smooths out site selectivity of the kinetics and the adatoms have an *effective* diffusion length which is potential dependent since it results from the competition between surface diffusion and desorption (figure 1(a)). Surface diffusion becomes an intrinsic property of the system under mass control limitations since the adatom is *irreversibly* adsorbed on the surface. Hence for large enough η, electrodeposition resembles very much MBE deposition and the same concepts of surface diffusion, island nucleation and growth apply. Depending on the deposition flux and adatom *effective* mobility, the adatom will reach favourable sites (like steps or other defects) or aggregate with other adatoms. An example of this mechanism is given by figure 2(c) where the nucleation is obviously homogeneous on the gold terraces.

3. Self-organized metallic nanostructures on metal substrates

As mentioned above, the self-organized electrochemical growth of metallic nanostructures relies on the possibility of preparing electrode surfaces with periodic surface heterogeneity. As described in the following, most of the results were obtained for Au(111) because it is relatively easy to prepare a clean and reconstructed Au(111) surface in air, with a structure identical to the one observed after annealing in UHV [34]. Success in using this surface for growing self-organized nanostructures is also bound to the fact that this structure can be stabilized under appropriate electrochemical conditions. The herringbone pattern in figure 3(a) has been observed in many aqueous electrolytes at potentials where no specific anion adsorption is occurring. The reconstruction is lifted into a (1×1) structure upon specific adsorption of anions [20]. Besides the Au(111) surface, there are only a few metals whose bare surface presents an interesting surface reconstruction pattern. As mentioned in the introduction, a periodic dislocation pattern was created in UHV on unreconstructed Pt(111) by depositing two silver monolayers [13]. This concept has been successfully transposed to the electrochemical interface with the same system. A 2 ML thick silver layer electrodeposited on Pt(111) generates
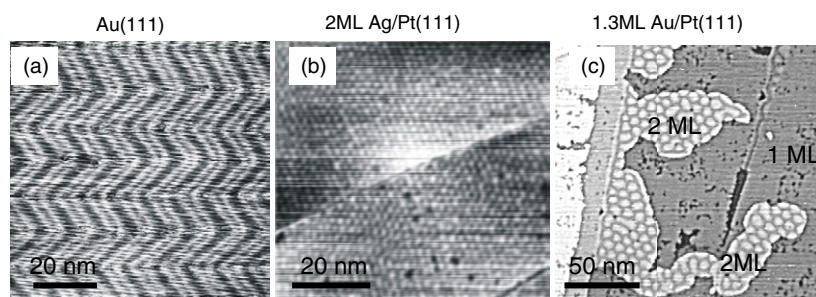
Figure 3. *In situ* STM images of different surfaces with ordered heterogeneity patterns. (a) 84 nm $\times$ 84 nm image of a Au(111) surface with the $22 \times \sqrt{3}$ reconstruction prepared by flame annealing ($U = 0$ V_{SCE} in 0.1 M $HClO_4$). (b) 65 nm $\times$ 65 nm image of a periodic dislocation network created by electrodeposition of 2 ML of silver at 0.04 V_{Ag/Ag^+} on Pt(111) from a 1 mM $AgNO_3$ solution [35]. (c) 180 nm $\times$ 180 nm image of a dislocation network created on top of 2 ML thick gold islands deposited from a 1 μM $KAuCl_4$ solution at 0.04 V_{AgCl} sat' [36]. The dislocations are the dark lines in (b) and (c).
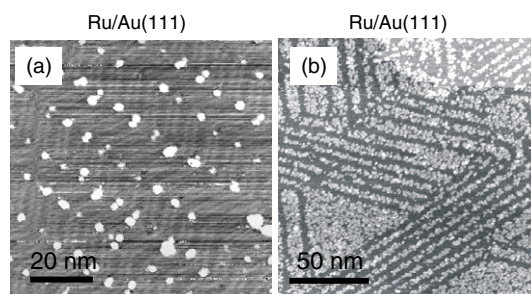
Figure 4. *In situ* STM images of self-ordered Ru deposits on Au(111) obtained under mass transport control at large overpotential [37]. (a) At low deposition flux, Ru nucleates preferentially at the elbows of the herringbone pattern of the reconstructed surface. (b) At higher flux, Ru nucleates on the fcc regions of the Au(111) surface reconstruction. Deposition was performed at 0 V_{SCE} from a 10 μM (a) and 100 μM (b) $RuCl_3$ solution. The image size is 85 nm $\times$ 85 nm (a) and 150 nm $\times$ 150 nm (b).

in fact a similar regular dislocation network (figure 3(b)) [35]. Gold gives rise to the same phenomenon on Pt(111) under appropriate surface polarization. The *in situ* STM image in figure 3(c) evidences a dislocation network in regions where the gold film is 2 ML thick at a sufficiently positive potential where sulfate anions adsorb (no superstructure is discernible in regions where the layer is only 1 ML thick) [36].

As discussed in section 2, electrodeposition may be realized in two different regimes. At very large overpotential the process is analogous to vacuum deposition because the adatom is irreversibly adsorbed and the deposition rate is controlled by the metal concentration in the solution (mass transport limitation). This technique was used to prepare self-ordered Ru nanostructures on reconstructed Au(111) terraces. At a low deposition flux, the Ru islands are decorating the elbows of the Au(111) reconstruction pattern which creates a regular array of Ru nanostructures. The process is driven by place exchange. The loosely bound Au atoms present at elbows of the herringbone reconstruction pattern are expelled from the surface plane and are replaced by Ru atoms which then act as preferential nucleation centres (figure 4(a)) [37]. This morphology is totally analogous to the UHV deposition of Ni, Co, Pd and Mo on Au(111) [9–12]. At a larger deposition flux, the Ru islands are formed on the fcc regions
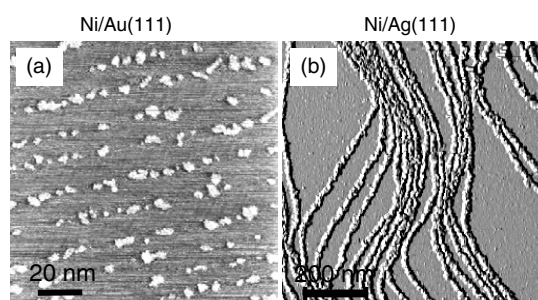
Figure 5. *In situ* STM image of Ni deposits obtained by *direct* deposition at low overpotential. (a) At sufficiently low deposition flux on Au(111) self-ordered growth of Ni islands is driven by place exchange at the elbows of the reconstruction pattern (image 120 nm × 120 nm) [39]. (b) On Ag(111), Ni lines form at steps (image 850 nm × 850 nm) [40].

of the reconstructed Au(111) surface figure 4(b). This behaviour is attributed to the faster Ru adatom diffusion on the hcp than on the fcc regions of the Au(111) reconstructed surface [38].

In contrast to the large overpotential regime case, *direct* electrodeposition occurs at low overpotential. Under these conditions, Ni electrodeposition [39] gives rise to the same array of self-ordered islands as described above for Ru (figure 5(a)): the nucleation of the nickel islands is again driven by place exchange. Observing this phenomenon requires a very small deposition flux because the place exchange is quite slow and it occurs in parallel with the direct deposition of the subsequent Ni adatoms at the island rim. For this reason the island size dispersion critically depends on the Au adatom mobility [39]. Ni electrochemical growth on Ag(111) is another typical example where the growth may be dominated by the *direct* discharge of the adatom at the step sites without adatom diffusion [40]. The perfect decoration of the silver steps observed in figure 5(b) arises from this specific mechanism. After the incorporation of the first metallic Ni adatoms at steps, one does not observe a step flow growth because the discharge of the next Ni adatom occurs directly on the Ni steps and on Ni itself. Within a specific potential range one may create nickel lines of several ML in height and few nm in width which are replicating the steps of the Ag(111) substrate [40]. This *direct* growth process has no equivalent in MBE growth and may be compared to reactive chemical vapour deposition.

4. Self-ordered metal electrodeposition on H-terminated silicon (111)

Unlike metals, a clean silicon surface is not stable outside a UHV chamber because the dangling bonds rapidly react with oxygen to form an oxide layer. Only surfaces with all surface bonds saturated, such as the 1×1 H–Si(111) surface, can exist both at ambient and in UHV. Vacuum metal deposition on 7×7 Si(111) and H-terminated (111) surfaces is now well documented [41]. 2D growth is generally observed on the clean surface with strong site selectivity inside the 7×7 surface unit cell and/or at steps [3–5]. The growth becomes generally 3D-like on the H termination [41] because of a lower surface energy and also because this surface is unreactive. The segregation of the H monolayer has been a subject of intense debate [41]. In some cases (e.g. iron), the first metal monolayer is indeed buried under the topmost atomic plane. Electrochemical metal growth on H-terminated Si(111) is expected to be 3D for the same energetic reasons. A 3D growth is moreover favoured because a preferential electrochemical transfer is expected at the deposited metal nuclei [42, 43]. In this section we will examine how strong site selectivity along the silicon steps may be obtained at the electrochemical interface on H–Si(111). Because this is of central interest for self-ordered electrochemical growth on
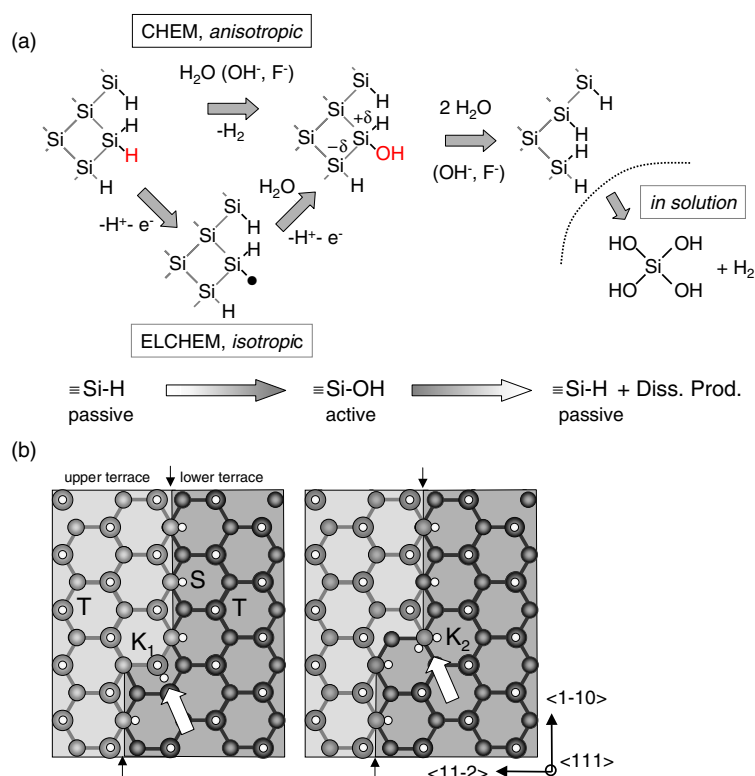
Figure 6. (a) Molecular scale mechanism for the silicon dissolution from a kink in an alkaline solution. In a fluoride containing solution, the initial OH group is rapidly substituted by a F atom [46]. (b) Atomic model showing the different surface sites and describing the removal of a kink site from a step on a H–Si(111) surface. The upper and lower terraces are respectively coloured in light grey and grey and the position of the atomic step is marked by arrows. Labels T, S, K_1 and K_2 in the figure refer respectively to terrace, step and kink sites. The two sorts of kink sites differ from the plane containing the two Si–H bonds. For K_1 this plane is vertical. It is oblique for K_2. The dissolution rate at sites K_1 and K_1 is about 10^2 larger than at sites S and 10^6 larger than at sites T.

silicon, the next subsection deals with the preparation of vicinal H-terminated silicon (111) surfaces with regularly spaced and straight steps.

4.1. Stepped silicon (111) surfaces obtained by 'chemical' etching

In UHV, a vicinal surface is obtained by using a specific annealing procedure to remove the oxide and promote surface restructuring thanks to surface diffusion and surface reconstruction at elevated temperature [3, 4, 41]. At ambient, the usual way of preparing silicon surfaces is chemical etching in fluoride media to strip the oxide layer and obtain a complete H termination of the surface [44]. The final surface structure results from the irreversible *removal* of tens of atomic layers by dissolution of the substrate. The challenge is hence promoting a site selective reaction to reveal well defined atomic planes. For the reasons given below, a stepped surface is only obtainable with Si(111) because the (111) planes are etch stop planes.

It is now well known that the silicon surface bonds are all saturated with one or several hydrogen atoms after oxide stripping in acidic HF [45]. On the molecular scale, the silicon dissolution has been modelled by several groups and a review on this subject may be found in [44]. Our description [46, 47] assumes that the dissolution begins with a surface substitution

Si–H → Si–OH (figure 6(a)). The OH group is then rapidly substituted by a F atom in a fluoride containing solution. This activates the surface because the Si–Si back-bonds are locally polarized. Rapid breaking of the Si–Si bonds follows by reaction with water molecules [46] or HF at low pH [47, 48]. The total reaction removes one silicon atom from the surface and it generates new surface Si–H bonds (molecular hydrogen is also formed). The first substitution step is rate determining which means that the persistence of the H termination during the reaction has a kinetic origin. Notice that, from a purely thermodynamic viewpoint, an Si–F or an Si–OH termination would be more favourable than Si–H since the bond energy is ∼6–7 eV for Si–F and only ∼3.5 eV for the Si–H bond [44].

After oxide stripping in acidic HF the topography of the surface is the fingerprint of the $Si(111)/SiO_2$ interface. It is rough on the atomic scale because silicon dissolves very slowly in HF. There exist four different kinds of atomic sites on this surface (see figure 6(b)), at which the individual rate of dissolution is only a function of sterical and conformational considerations since we recall that all sites are chemically equivalent (all surface bonds are saturated with H atoms). Preparing a stepped Si(111) surface by chemical etching requires therefore conditions where the dissolution rate is much faster at kinks and step sites than on the (111) terraces. Given the reaction mechanism above (figure 6(a)) the key is controlling the *partition* between the two pathways accounting for the rate determining step Si–H → Si–X [46, 47]. Namely the chemical route Si–H + H_2O → Si–OH + H_2 (top route) must be favoured because it is highly anisotropic for steric reasons. It preferentially occurs at the step edges because the water molecule may freely adopt an adequate orientation and come into close proximity with the Si–H bond to react with it. The Si–H bond energy is also weaker at kink sites and step monohydrides than at terrace monohydrides. In contrast, the electrochemical pathway (bottom loop in figure 6(a)) is much less site dependent. At the rest potential the desorption of the H atoms is thought to be more homogeneous since it is catalysed by interaction with the electron donor anions F^- or OH^- in the solution [46, 47]. The resulting reactive sites $Si^\bullet$ are rapidly transformed into silanol groups which are etched away as described above. The electrochemical component of the dissolution must therefore be hindered as much as possible to obtain a stepped surface. There are different control parameters for achieving this goal. One is applying an external potential to the silicon substrate to accumulate electrons at the surface which totally stops the electrochemical dissolution. A perfect step flow etching was observed by *in situ* STM in such conditions of polarization in 2M NaOH, whereas strong and fast pitting occurred at the rest potential [49]. To reduce pitting at the rest potential or under so-called 'chemical' etching conditions (no external potential applied) the pH of the fluoride solution is the main control parameter because the rate of the chemical route increases with increasing pH, while, at the same time, the rate of the electrochemical route is only weakly pH dependent [46]. Increasing the solution pH therefore increases the anisotropy of the dissolution and a good compromise is experimentally using a buffer 40% NH_4F (pH 8) solution [50].

Since Chabal's discovery, the protocol for silicon etching in NH_4F has evolved remarkably to give quasi-perfect surfaces [51–54]. A major improvement has been the suppression of the dissolved oxygen from the etching solution, which lies at the origin of the large and deep triangular etch pits shown in figure 7(b). The second improvement came from the introduction of a sacrificial anodic area on the sample (see figure 7(c)) to suppress the residual electrochemical reaction of dissolution at the polished face of the wafer. Under these strict experimental conditions perfectly smooth (111) terraces develop with time as shown in figures 7(d), even though the array of step edges is still very much disordered. In this image one nevertheless notices that portions of the steps are quite rectilinear. This is because the kinks dissolve at a much faster rate than monohydride step sites (figure 6(b)). A quantitative analysis of *in situ* STM observations has shown that the rate of dissolution at kinks is about
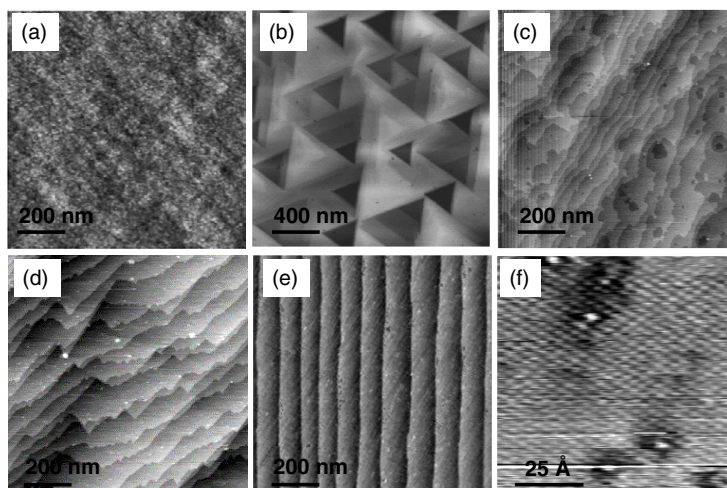
Figure 7. Topography of Si(111) surfaces with a miscut angle 0.2°. (a) *Ex situ* AFM image of the surface after oxide stripping in acidic HF. Note the atomic roughness. (b) Same as (a) but after etching in 40% NH_4F in the presence of dissolved molecular oxygen. (c) Same as (b) but in the absence of oxygen using a double-side-polished wafer. (d) Same as (c) but for a sample with one unpolished face and uncontrolled miscut orientation. (e) Same as (d) but for a miscut precisely oriented towards $\langle 11\bar{2} \rangle$. Note the perfect stepped structure. (f) *In situ* STM image showing the 1×1 H termination on a (111) terrace ($U = -2$ V in NaOH). The white protrusions are isolated OH sites, which modify the local density of states and the potential distribution. Images (a)–(e) are taken from [54] and (f) from [57].

10^2 faster than that at step monohydride sites [55]. The comparison of surface morphology with KMC simulations has confirmed this value and showed that the rate of dissolution is 10^6 to 10^7 slower at terrace sites than at kinks [56]. This huge difference arises from the specific chemical dissolution mechanism (top route in figure 6(a)). A precise *orientation* of the miscut towards $\langle 11\bar{2} \rangle$ is therefore a prerequisite for obtaining straight steps or, equivalently, obtaining steps terminated by monohydride step sites. In that case figure 7(e) shows that a quasi-perfect staircase structure may be prepared, with atomically flat (111) terraces separated by atomic steps corresponding to one silicon bilayer ($h = 3.14$ Å) [54]. It is worth recalling that several nm of material have been dissolved within 15 min, since we started from a rough surface like the one in image 7(a), to reach a steady state step flow etching (the etching rate is $\sim$0.2–0.5 nm min^{-1} in NH_4F [46]). With such a precisely cut crystal, the step density is only a function of the tilt angle and it is highly uniform across the sample. Zooming on one terrace with an *in situ* STM tip (figure 7(f)) reveals the expected (1×1)-H structure and some isolated OH groups [57], whose appearance arises from both an increased local density of states (the corresponding protrusion is higher than expected from the bond geometry) and a locally modified potential distribution at the surface (see the dark crown around the OH group). Finally, we would like to point out that the same result may be obtained by etching the silicon in oxygen free water [58], which gives credibility to the mechanism of dissolution above in which molecular water is indeed the oxidizing species while OH$^-$ or F$^-$ ions are only catalysts of the reaction at medium pH.

4.2. Arrays of gold dots produced by electrodeposition on stepped silicon

Before starting the discussion, we inform the reader that various textbooks address the principles of semiconductor electrochemistry [29] and that a very complete book is also
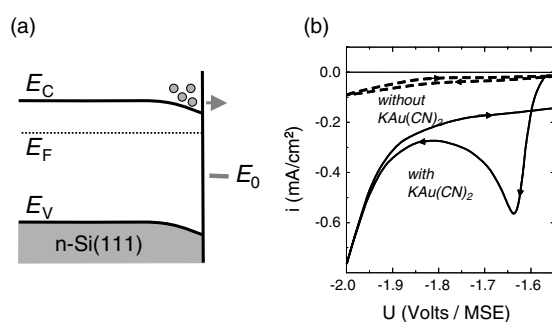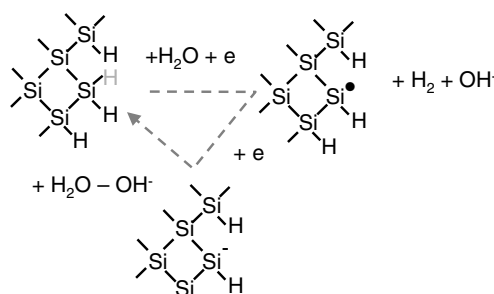
Figure 8. Gold electrodeposition on n-type H–Si(111) from a KAu(CN)$_2$ solution (pH 14). (a) Energy diagram of the n-type silicon–electrolyte junction during deposition. The junction is in the direct polarization condition, to accumulate electrons (grey dots) in the conduction band at the surface from where they are transferred onto the gold complexes. (b) Cyclic voltammetry: the dashed and solid lines refer to the gold free and gold containing solutions (after [59]).
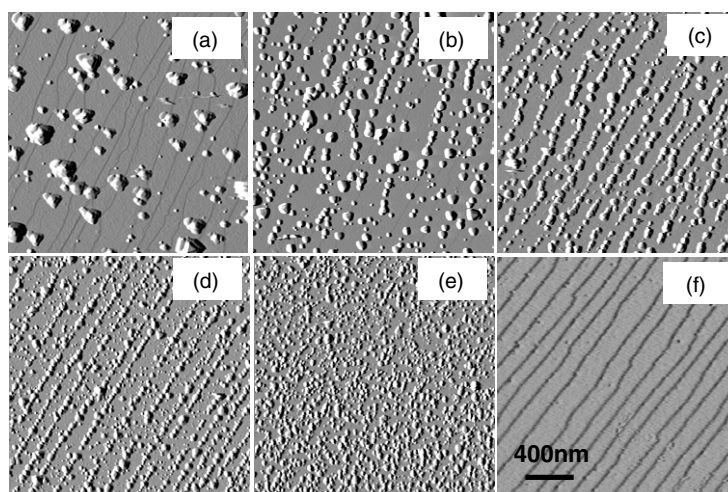
Figure 9. AFM observations after the deposition of about 10 ML of gold at -1.6 V (a), -1.7 V (b), -1.75 V (c), -1.8 V (d), -1.9 V (e) [59]. The initial surface is shown in (f). All frames are 2 μm $\times$ 2 μm. At -1.75 V a large density of islands is obtained at the silicon steps while there is no significant nucleation on the terraces.

available on silicon electrochemistry [44]. We only mention here that the semiconductor–electrolyte interface behaves like a Schottky contact, with the solution playing the role of the metal. For this reason, one must apply a more negative potential at a semiconductor electrode than at a metal–solution interface to promote a given cathodic reaction. This is to lower the built-in surface barrier and allow transfer of conduction band electrons by thermionic emission towards the metal ions, as schematically shown in figure 8(a) in the case of gold electrodeposition on an n-type Si(111) electrode from a gold cyanide solution (KAu(CN)$_2$). The negative peak of current at -1.6 V (figure 8(b)) corresponds to the reduction of the gold complex Au(CN)$_2^-$ (E(Au$^+$/Au) $= -1.25$ V$_{\text{MSE}}$). The decomposition of water, which is occurring in parallel, appeared to be a key issue as regards the metal nucleation.

Gold nucleation from this solution is highly selective at the silicon steps [59] when the deposition potential ranges between the nucleation onset potential -1.55 and -1.75 V. In

Figure 10. Reaction scheme for the decomposition of water or HER on an n-type H–Si(111) electrode (after [49]). Note the H desorption stage and the regeneration of the Si–H bond, with the production of one molecule of H_2. This scheme explains that self-ordered growth of gold on stepped Si(111) is coupled with the site selectivity of the HER.

figures 9(a)–(c), the nm gold islands are all positioned across the silicon steps and one only varies their density along the steps by applying a more negative potential (figures 9(a)–(c)). At a potential of −1.75 V (figure 9(c)) the gold nuclei are densely aligned in parallel lines whose separation distance matches exactly the mean distance between the atomic steps of the H–Si(111) surface (figure 9(f)). This quasi-exclusive site selectivity is induced by the co-reduction reaction of water into molecular H_2, a reaction which occurs in parallel with metal deposition. On the molecular scale the total reaction $H_2O + e^- \rightarrow \frac{1}{2}H_2 + OH^-$ may be decomposed into several elementary steps (figure 10) [49]: in the first one a first H_2O molecule breaks a Si–H bond, which generates a reactive site $Si^\bullet$ with an unpaired electron. The Si–H bond is formed again after the capture of a second conduction band electron by the $Si^\bullet$ site and by the abstraction of an H atom from a solvent molecule. For the steric reasons discussed above in the case of the etching reaction (figure 6(a)), the decomposition of water is faster at step sites. As a result of the preferential formation of active sites $Si^\bullet$ at steps, the gold species are preferentially discharged there and Si–Au bonds formed at steps. The Au–Si sites are then acting as preferential nucleation centres for further self-ordered growth of gold[2]. The process is quite slow during the initial stages as evidenced by the size dispersion of the gold islands. Significant gold nucleation on the (111) terraces can nevertheless be obtained by applying more negative potentials to promote water decomposition on the (111) terraces (figures 9(d) and (e)).

To improve the size dispersion of the gold islands at steps, one must decouple the nucleation stage from the growth by using 'double-potential-step electrodeposition' [60]. In this procedure, the first step of potential controls the density of nuclei along the silicon steps and the second one allows the growth of the existing nuclei. In the case of gold growth on stepped H–Si(111), the optimum sequence is applying −2 V for few seconds, to promote strong hydrogen evolution reaction (HER) at the silicon steps and saturate them with gold nuclei, and then −1.5 V for several tens of seconds, to grow the gold islands at will without nucleating new islands (see figure 11). Thus fabricated deposits (figure 11(b)) consist of rather monodisperse gold islands with $2\ 10^5$ islands cm^{-1} along the steps, which is equivalent to a mean spacing 50 nm between the centres of islands. Experimentally this linear density is close to saturation for reasons which seem intrinsic to electrochemical deposition on a semiconductor. From a structural viewpoint [59] the Au islands are flat top (111) nanocrystals positioned across the silicon steps (figure 12(a)) and they are in epitaxy with the substrate according to

---

[2] A test of the nucleation model consisted in lowering the solution pH to 4 to make the HER site insensitive (at this pH, protons directly recombine with H atoms from the surface). In these conditions a homogeneous nucleation of gold clusters is observed on the Si(111) terraces.
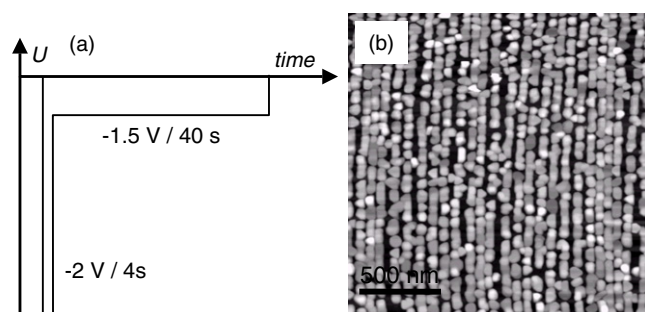
Figure 11. (a) Principle of double-potential-step electrodeposition: the first and short step at high overpotential controls the nucleation and the second step controls the growth of the islands. (b) Morphology of a deposit grown with the sequence -2 V for 4 s and then at -1.5 V for 150 s (image $2~\mu\text{m} \times 2~\mu\text{m}$) [60]. The substrate is n-type Si(111) with a miscut $0.2°$. Note the improved size distribution of the Au islands with respect to figure 9(c).
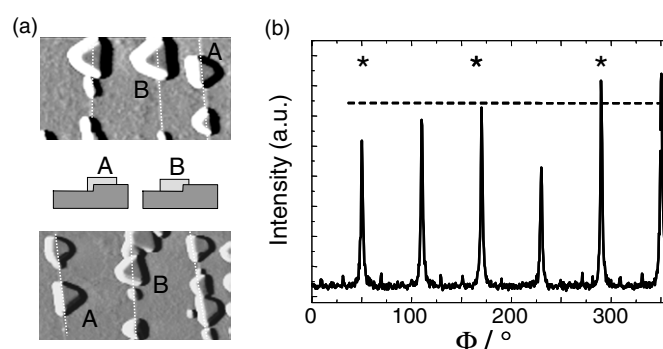

Figure 12. (a) Two 180 nm $\times$ 130 nm AFM image showing that the gold islands are flat top and present a well defined geometrical shape [59]. (b) Grazing incidence XRD spectrum showing the excellent epitaxy between the (111) gold clusters and the Si(111) crystal. The peak FWHM is $\sim2°$. Peaks marked with a (*) correspond to Au(111) islands which are aligned with Si(111) (after [59]).

the relationship Au(111)[1$\bar{1}$0] $\parallel$ Si(111)[1$\bar{1}$0] as indicated by the XRD diffraction spectrum in figure 12(b). The sixfold symmetry of the spectrum reflects the hexagonal symmetry of the silicon surface. This excellent epitaxy is attributed to the progressive removal of the 'hydrogen carpet' from the H–Si(111) terrace from the boundary between the H monolayer and the edges of the growing gold clusters. Above a critical island size, 3D growth takes over by preferential electrochemical transfer through the locally more active metal clusters (compared to the remaining H-terminated surface) [59].

We used such an array (table 1) as a template for fabricating magnetic nanostructures by template electrodeposition of a ferromagnetic metal atop the gold clusters [61]. Compared to its counterpart UHV approach, which was presented at the conference on clean Si(111),[3] one advantage of the electrochemical growth is the possibility of growing cobalt onto gold without depositing any cobalt onto the bare silicon surface remaining between the Au islands. In figure 13(a) we compare the voltammograms of the bare and Au covered silicon electrode.

---

[3] A poster presented by Agnus *et al* at the conference showed that an array of Co/Au dots can also be prepared on a vicinal 7×7 Si(111) *clean* surface. The technique requires an additional thermal treatment to transform the cobalt layer into a silicide layer between the gold islands.
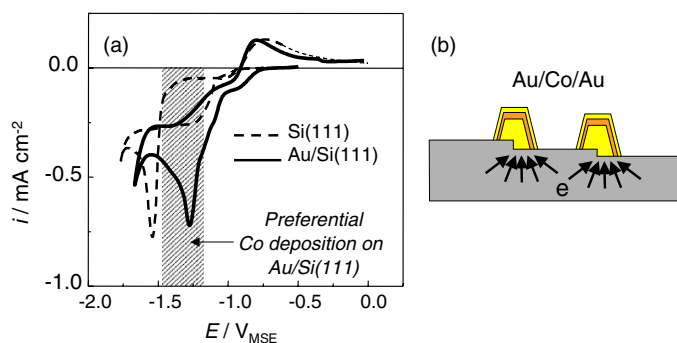
Figure 13. Preparation of Au/Co/Au dots by template cobalt growth on the Au dots [61]. (a) Voltammograms of the H-terminated (dashed line) and Au covered (solid line) n-type Si(111) electrode showing that Co may be selectively deposited on the Au dots by applying the potential within the hatched area. (b) Schematic cross section of the sample showing the internal structure of the Au/Co/Au dots decorating the steps.

Table 1. Physical dimensions and magnetic characteristics of the array formed by Au(111) clusters on stepped silicon with a miscut 0.2° [60, 61].

Physical dimensions	
Array dimension	Approx. 50 nm × 100 nm
Surface density	$D \sim 2.5 \times 10^{10}$ cm^{-2}
	(adjustable by changing the step density)
Diameter	$d \sim 32$ nm (adjustable with deposition time)
Aspect ratio	$h/d \sim 0.4$ ($h \sim 12$ nm ~ 50 ML/dot)
Magnetic properties	
3 ML Co/dot	Uniaxial anisotropy perpendicular to the surface
10 ML/dot	In-plane uniaxial anisotropy parallel to steps

They evidence that exclusive cobalt deposition atop the Au islands takes place within the hatched potential window as no cobalt is deposited on bare silicon at such potentials: namely, in this potential range, the electrons are preferentially transferred to Co^{2+} ions through the deposited Au islands which leads to the island structure sketched in figure 13(b). A capping of gold was, in the same way, deposited onto cobalt to protect the ultrathin ferromagnetic layer against oxidation in air. Because the Au islands are (111) nanocrystals with a flat top and (111) facets the knowledge about Co/Au(111) growth applies [31, 32]. In particular, the Co layer is found to be (0001) oriented from x-ray diffraction. From a magnetic viewpoint the dot array is ferromagnetic at room temperature and presents, in the case of Si(111) with a miscut 0.2° (table 1), uniaxial magnetic properties which vary with the cobalt thickness, expressed in ML per dot in the following [61]. For 3 ML of cobalt a square $M–H$ hysteresis loop (figure 14(a)) was measured using the polar magneto-optical Kerr effect (PMOKE), which is a signature of a perpendicular magnetization anisotropy. Increasing the cobalt thickness to 20 ML brings the easy magnetization into the plane of the surface. This rotation phenomenon is similar to the one observed at two-dimensional electrodeposited Cu/Co/Au(111) layers [31]. The big difference is however that the dot array presents an in-plane uniaxial anisotropy. The $M–H$ loop in figure 14(b) is indeed square when the in-plane external field is parallel to the dense direction of islands or parallel to the step direction (solid line): the dipolar coupling is strong enough between the islands along one silicon step to keep all the individual spins parallel to
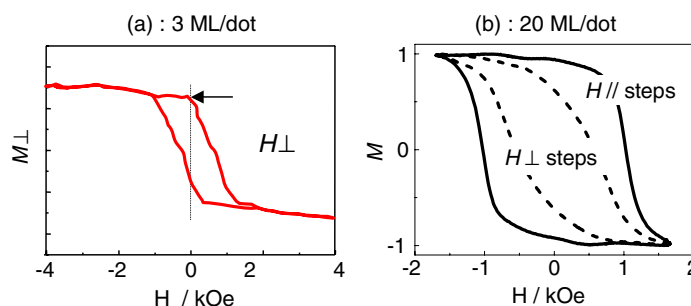
Figure 14. Magnetic properties a Au/Co/Au dot array grown on Si(111) with a miscut 0.2° (table 1) [61]. (a) 3 ML of cobalt/dot: M–H hysteresis loop (PMOKE measurement) showing that the magnetization is out of the plane for this cobalt thickness. (b) 20 ML of cobalt/dot: M–H hysteresis loops (MOKE measurement) showing that the magnetization easy axis is in the plane. Note the uniaxial anisotropy along the silicon steps as evidenced from the different coercive fields with the external field parallel (solid line) or perpendicular (dotted line) to the step edge direction.

the silicon step upon decreasing the external field from the saturation state. Each line of dots behaves therefore like a magnetic nanowire although the dots are not physically connected as observed by SEM. When the field is applied perpendicular to the silicon steps (figure 14(b), dotted line) the coercive field is smaller by a factor of 2 than with the field parallel to the step direction (figure 14(b), solid line). The remnant magnetization is also smaller in the latter case. This difference indicates that the dipolar interactions between the magnetic dots are smaller when they are located on two different steps. In fact, the average nearest distance between the dots is 100 nm when the dots are located on different silicon steps whereas it is 50 nm when the dots are located on the same silicon step (table 1).

Before closing this section we would like to mention that other works have shown that metal electrodeposition on silicon can be performed at the rest or free potential. This technique relates to electroless deposition because the net current flow is equal to zero: the substrate dissolution current (anodic) is compensated by the cathodic current associated with metal deposition. This technique is more difficult and less well controlled than cathodic electrodeposition, in particular because the metal nucleation critically depends on the pH of the electrolyte, which is often a fluoride solution, and on the metal concentration. At low pH and for metals with a standard potential $E(M^{z+}/M)$ *inside* the band gap, such as for the system HF–NiSO$_4$ solution [62], deposition is difficult because the silicon dissolution is very slow at this pH [46]. For those metals with a standard potential $E(M^{z+}/M)$ *below* the valence band of silicon, such as gold and platinum, the deposition from a HF solution occurs by capture of valence band electrons and the homogeneous substrate dissolution leads to a uniform metal nucleation [63, 64]. To promote step edge decoration one must increase the pH to enhance the anisotropic component of the etching (top route in figure 6(a)) and reduce as much as possible the metal concentration. For instance copper electroless deposition from an oxygen free 40% NH$_4$F solution occurs preferentially at silicon steps of a H–Si(111) surface [65] because the Cu$^+$ ions, which are intermediate of the reaction, are chelated by the dihydroxyl groups at kink sites (see figure 6(a)). These surface complexes act as preferential centres for the reduction of Cu^{2+} by transfer of conduction band electrons (the standard potential $E(Cu^{2+}/Cu)$ lies in the gap as in figure 8). The density of islands remains however quite small and the steps are far from being saturated with the metal nuclei because site selective deposition requires very diluted solutions (in the μM range) to avoid significant electrochemical dissolution on the terraces (bottom route in figure 6(a)). Using a copper solution in oxygen free water instead of NH$_4$F

seems to give much better results. Cu clusters and nanowires were indeed grown on stepped H–Si(111) from 100 ppb CuSO$_4$ dissolved in ultrapure water [66]. In this case the reduction of the metal species is uniquely connected with the anisotropic dissolution chemical route at steps (top route in figure 6(a)) and the electrochemical dissolution is essentially stopped.

In conclusion of this section the electrochemical mechanism of nucleation of metals on H-terminated silicon appears to be quite specific and has no equivalent in UHV. The observed site selective nucleation is indeed intimately connected with the preferential H desorption from the silicon steps, a phenomenon which may be induced either by the HER (the case of cathodic deposition) or by the dissolution (the case of electroless deposition). As a result quite different growth modes can be obtained on H–Si(111) at the electrochemical interface compared to those observed in UHV [41].

5. Conclusions

In this brief review we have shown that electrochemical deposition is a versatile technique, which allows growing self-organized nanostructures. One interesting feature of electrodeposition is that different nucleation and growth modes are attainable for a given metal by adjusting the solution composition and the applied potential. Likewise, in UHV conditions, self-ordered electrochemical growth requires surfaces with ordered arrays of preferential nucleation centres and progress in this direction is subject to work dedicated to the preparation of substrates with well defined surface patterns, an effort which was successful with Au(111) and H–Si(111) but remains a challenge with other substrates. The examples discussed in this paper illustrate also some specificity of electrochemical nucleation, especially with the existence of a direct deposition process which has no equivalent in vacuum.

Acknowledgments

References

[1] See for instance IWGN workshop report available at: http://www.wtec.org/loyola/nano/IWGN.Research.Directions/
[2] Kotlyar V G, Zotov A V, Saranin A A, Kasyanova T V, Cherevik M A, Pisarenko I V and Lifshits V G 2002 *Phys. Rev.* B **66** 165401
    Lai1 M Y and Wang Y L 2001 *Phys. Rev.* B **64** 241404
    Li J-L, Jia J-F, Liang X-J, Liu X, Wang J-Z, Xue Q-K, Li Z-Q, Tse J S, Zhang Z and Zhang S B 2002 *Phys. Rev. Lett.* **88** 066101
[3] see for instance Himpsel F J, McChesney J L, Crain J N, Kirakosian A, Perez-Dieste V, Abbott N L, Luk Y-Y, Nealey P F and Petrovykh D Y 2004 *J. Phys. Chem.* B **108** 14484 and reference therein
[4] Sekigushi T, Yoshida S and Itoh K M 2005 *Phys. Rev. Lett.* **95** 106101
[5] Gonzalez C, Snijders P C, Ortega J, Perez R, Flores F, Rogge S and Weitering H H 2004 *Phys. Rev. Lett.* **93** 126106

[6] Gambardella P, Blanc M, Brune H, Kuhnke K and Kern K 2000 *Phys. Rev.* B **61** 2254
[7] Repain V, Berroir J M, Rousset S and Lecoeur J 2000 *Surf. Sci.* **447** L152
    Weiss N, Cren T, Epple M, Rusponi S, Baudot G, Rohart S, Tejeda A, Repain V, Rousset S, Ohresser P, Scheurer F, Bencok P and Brune H 2005 *Phys. Rev. Lett.* **95** 157204
[8] Meyer J A, Baikie I D, Kopatzki E and Behm R J 1996 *Surf. Sci.* **365** L647
[9] Chambliss D D, Wilson R J and Chiang S 1991 *Phys. Rev. Lett.* **66** 1721
[10] Voigtländer B, Meyer G and Amer N M 1991 *Phys. Rev.* B **44** 10354
[11] Stephenson A W, Baddeley C J, Tikhov M S and Lambert R M 1998 *Surf. Sci.* **398** 172
[12] Helveg S, Lauritsen J V, Laegsgaard E, Stensgaard I, Norskiv J K, Clausen B S, Topsoe H and Besenbacher F 2000 *Phys. Rev. Lett.* **84** 951
[13] Röder H, Bromann K, Brune H and Kern K 1997 *Surf. Sci.* **376** 13
[14] Brune H, Giovannini M, Bromann K and Kern K 1998 *Nature* **394** 451
[15] Ellmer H, Repain V, Sotto M and Rousset S 2002 *Surf. Sci.* **511** 183
[16] Jakob P, Gesell M and Menzler D 2001 *J. Chem. Phys.* **114** 10075
[17] Clavilier J, Faure R, Guinet G and Durand R 1980 *J. Electroanal. Chem.* **107** 205
[18] Gewirth A A and Niece B K 1997 *Chem. Rev.* **97** 1129
[19] Itaya K 1998 *Prog. Surf. Sci.* **58** 121
[20] Magnussen O M 2002 *Chem. Rev.* **102** 679
[21] Kolb D M 2002 An atomistic view of electrochemistry *Surf. Sci.* **500** 722
[22] Allongue P 1995 *Scanning Tunneling Microscopy of Semiconductor Electrodes* (*Advances in Electrochemical Science and Engineering* vol 4) ed H Gerischer and C W Tobias (Weinheim: VCH) p 1
[23] Henry Y, Iovan A, George J M and Piraux L 2002 *Phys. Rev.* B **66** 184430
[24] Ross C A, Haratani S, Castañõ F J, Hao Y, Hwang M, Shima M, Cheng J Y, Vögeli B, Farhoud M, Walsh M and Smith H I 2002 *J. Appl. Phys.* **91** 6848
[25] Zheng M, Menon L, Zeng H, Liu Y, Bandyopadhyay S, Kirby R D and Sellmyer D J 2000 *Phys. Rev.* B **62** 12282
[26] Martin C R 1994 *Science* **266** 1961
[27] Asoh H, Nishio K, Nakao M, Tamamura T and Masuda H 2001 *J. Electrochem. Soc.* **148** B152
[28] Bartlett P N, Birkin P R and Ghanem M 2000 *Chem. Commun.* 1671
[29] Bard A J and Faulkner L R 2001 *Electrochemical Methods* 2nd edn (New York: Wiley)
[30] Maroun F and Allongue P, unpublished data
[31] Cagnon L, Devolder T, Cortes R, Schmidt J E, Chappert C and Allongue P 2001 *Phys. Rev.* B **63** 104419
[32] Allongue P, Cagnon L, Gomes C, Gündel A and Costa V 2004 *Surf. Sci.* **557** 21
[33] Cagnon L, Gündel A, Devolder T, Morrone A, Chappert C, Schmidt J E and Allongue P 2000 *Appl. Surf. Sci.* **164** 22
[34] Barth J V, Brune H, Ertl G and Behm R J 1990 *Phys. Rev.* B **42** 9307
[35] Maroun F, Magnussen O M and Behm R J, unpublished
[36] Sibert E, Ozanam F, Maroun F, Magnussen O M and Behm R J 2003 *Phys. Rev. Lett.* **90** 056102
[37] Maroun F, Magnussen O M and Behm R J, unpublished
[38] Strbac S, Magnussen O M and Behm R J 1999 *Phys. Rev. Lett.* **83** 3246
[39] Möller F A, Magnussen O M and Behm R J 1996 *Phys. Rev. Lett.* **77** 5249
[40] Morin S, Lachenwitzer A, Magnussen O M and Behm R J 1999 *Phys. Rev. Lett.* **83** 5066
[41] for an extensive review on this subject see Oura K, Lifshits V G, Saranin A A, Zotov A V and Katayama M 1999 *Surf. Sci. Rep.* **35** 1
[42] Allongue P 1992 *Modern Aspects of Electrochemistry* (*Physics and Applications of Semiconductor Electrodes Covered with Metal Clusters* 23) ed B E Conway (New York: Plenum) chapter 4, pp 239–31
[43] Allongue P and Souteyrand E 1989 *J. Electroanal. Chem.* **269** 361–74
[44] Zhang X G 2001 *Electrochemistry of Silicon and its Oxide* (New York: Kluwer–Academic)
[45] Chabal Y J, Higashi G S, Raghavachari K and Burrows V A 1989 *J. Vac. Sci. Technol.* A **7** 2104
[46] Allongue P, Kieling V and Gerischer H 1993 *Electrochim. J. Electrochem. Soc.* **140** 1018
    Allongue P, Kieling V and Gerischer H 1995 *Electrochim. Acta* **40** 1353–60
[47] Gerischer H, Allongue P and Costa Kieling V 1993 *Phys. Chem.* **97** 753–7
[48] Trucks G W, Raghavachari K, Higashi G S and Chabal Y J 1990 *Phys. Rev. Lett.* **65** 504
[49] Allongue P, Kieling V and Gerischer H 1993 *J. Electrochem. Soc.* **140** 1009–26
[50] Higashi G S, Chabal Y J, Trucks G W and Raghavachari K 1990 *Appl. Phys. Lett.* **56** 656
    Jakob P and Chabal Y J 1991 *J. Chem. Phys.* **97** 2897
[51] Wade C P and Chidsey C E D 1997 *Appl. Phys. Lett.* **71** 1679
[52] Fukidome H and Matsumura M 1998 *Appl. Surf. Sci.* **130–132** 146
[53] Allongue P, Henry de Villeneuve C, Morin S, Boukherroub R and Wayner D 2000 *Electrochim. Acta* **45** 4591

[54] Munford M L, Cortes R and Allongue P 2001 *Sensors Mater.* **13** 259–69
[55] Kasparian J, Elwenspoek M and Allongue P 1997 *Surf. Sci.* **388** 50–62
[56] Flidr J, Huang Y-C, Newton T A and Hines M 1998 *J. Chem. Phys.* **108** 5542
[57] Allongue P 1996 *Phys. Rev. Lett.* **77** 1986–9
[58] Fukidome H and Matsumura M 1998 *Japan. J. Appl. Phys.* **38** L1085
[59] Munford M L, Maroun F, Cortes R and Allongue P 2003 *Surf. Sci.* **537** 95
[60] Gubi M, Maroun F and Allongue P, unpublished data
[61] Tisserand J C, Savidand G, Maroun F and Allongue P 2006 unpublished data
[62] Gorostiza P, Kulandainathan M, Diaz R, Sanz F, Allongue P and Morante J R 2000 *J. Electrochem. Soc.* **147** 1026
[63] Gorostiza P, Allongue P, Diaz R, Morante J R and Sanz F 2003 *J. Phys. Chem.* B **107** 6454
[64] Warren S, Reitzle A, Kazimirov A, Ziegler J C, Bunk O, Cao L X, Renner F U, Kolb D M, Bedzyk M J and
      Zegenhagen J 2002 *Surf. Sci.* **496** 287
[65] Homma T, Wade C P and Chidsey C E D 1998 *J. Phys. Chem.* B **102** 7919
[66] Tokuda N, Hojo D, Yamasaki S, Miri K and Yamabe K 2003 *Japan. J. Appl. Phys.* **42** L1210
      Hojo D, Tokuda N and Yamabe K 2003 *Japan. J. Appl. Phys.* **42** L581